DISCLAIMER

ORNL/TM-2025/3998

Laser Powder Bed Fusion Manufactured Alloys 625 and 282 and Properties Relevant to Advanced Nuclear Components

Sebastien Dryepondt
Holden Hyer
Amanda Heimbrook
Rahul Franklin
Amir Ziabari
Yi-Feng Su
Chase Joslin

July 2025

M3MT-25OR0902071

ORNL/TM-2025/3998

Advanced Materials and Manufacturing Technologies

LASER POWDER BED FUSION MANUFACTURED ALLOYS 625, 244, AND 282 AND PROPERTIES RELEVANT TO ADVANCED NUCLEAR COMPONENTS

Sebastien Dryepondt
Holden Hyer
Amanda Heimbrook
Rahul Franklin
Amir Ziabari
Yi-Feng Su
Chase Joslin

July 2025

M3MT-25OR0902071

Prepared by
OAK RIDGE NATIONAL LABORATORY
Oak Ridge, TN 37831
managed by
UT-BATTELLE LLC
for the
US DEPARTMENT OF ENERGY
under contract DE-AC05-00OR22725

CONTENTS

LIST OF FIGURES

LIST OF TABLES

ABBREVIATIONS

282	Haynes 282
625	Inconel 625
AM	additive manufacturing
AMMT	Advanced Materials and Manufacturing Technologies
BD	build direction
DMSCNN	dynamic multilabel segmentation convolutional neural network
EBSD	electron backscatter diffraction
EDS	energy-dispersive x-ray spectroscopy
GB	grain boundary
INL	Idaho National Laboratory
LPBF	laser powder bed fusion
ORNL	Oak Ridge National Laboratory
STEM	scanning transmission electron microscopy
TTT	temperature–time–transformation
UTS	ultimate tensile strength
XCT	x-ray computed tomography
YS	yield strength

ACKNOWLEDGMENTS

The authors would like to thank K. Carver, J. Moser, B. Abbott, D. Newberry, and T. Lowe for their help with the experimental work and acknowledge C. Massey for carefully reviewing the manuscript. This research was funded by the US Department of Energy Office of Nuclear Energy's Advanced Materials and Manufacturing Technologies program.

ABSTRACT

Under the Advanced Materials and Manufacturing Technologies program, two Ni-based alloys fabricated by laser powder bed fusion (LPBF) have been evaluated: γ′-strengthened Haynes 282 and solution-strengthened Inconel 625. Large printing defects were observed in the LPBF 282 alloy fabricated using a Renishaw AM250 machine, likely due to particle spattering during printing. Annealing at 1,180°C for 1 h followed by 4 h at 800°C in a high density of 50 nm γ′-strengthening precipitates as well as partial recrystallization resulted in a bimodal grain distribution. Creep testing performed at 750°C revealed lower creep life and ductility for the LPBF 282 compared with wrought 282. X-ray computed tomography combined with optical and scanning electron microscopy microstructural characterization revealed crack formation during creep testing, initiated either from printing defects or from creep cavitation at grain boundaries. Printing defects were the likely reason for the lower creep performance of LPBF 282 and could be suppressed by optimizing the build configuration.

Printing 625 on an EOS M290 machine using the recommended EOS parameters resulted in a very low defect density. Superior creep strength at 725°C was observed for the as-printed LPBF 625 along the build direction when compared with wrought 625. No defect larger than ~50 μm could be detected by X-ray computed tomography in the as-printed conditions and after creep testing for 1,000 h at 725°C and 150 MPa. Small, needle-like δ-phase precipitates were observed after creep testing for 100 h at 725°C and 200 MPa. The rapid formation of the γ phase is directly related to the initial Nb and Mo segregation in the LPBF 625 cell walls, and its effect on the alloy's high-temperature performance will be evaluated. Solution annealing was carried out at 1,150°C for 1 h and led to full recrystallization of the alloy. A decrease in strength and increase in ductility were observed after solution annealing, and the alloy recrystallization resulted in isotropic tensile properties at room temperature, contrary to what was observed for the as-printed LPBF 625.

1. INTRODUCTION

A key attribute of additive manufacturing (AM) techniques, such as laser powder bed fusion (LPBF), is the ability to fabricate complex, near net shape components [1]. Combinations of sensor outputs and health monitoring streams collected during LPBF can be used to create an AI-powered advanced diagnostic tool to elevate the position of AM for component qualification [2–3]. The US Department of Energy's Advanced Materials and Manufacturing Technologies (AMMT) program is taking advantage of this unique opportunity using AM for rapid qualification of new materials for light-water reactors and advanced reactor concepts [4]. Although stainless steel 316H fabricated by LPBF has been a key focus of the AMMT program [5–7], Ni-based alloys exhibit exceptional mechanical and corrosion properties at operational temperatures needed for high-performance advanced reactor concepts [8]. Oak Ridge National Laboratory (ORNL) and Idaho National Laboratory (INL) have been investigating AM fabrication and using several Ni-based alloys considering three key potential applications: (1) low-Co alloys to be used close to the reactor core, which has a high temperature; (2) high-strength alloys, enabling a higher operating temperature; and (3) low-Cr alloys compatible with fluoride and chloride molten salts [9]. Previous work concluded that LPBF Inconel 625 (abbreviated 625 in this report) was of particular interest as a printable, low-Co alloy with satisfactory high-temperature mechanical and corrosion resistance [10–11]. As a major alloy in the gas turbine and aerospace industries, extensive studies have been conducted on LPBF 625, from detailed microstructure characterization to performance evaluation and fabrication of complex geometries [12–24]. Additionally, wrought 625 is also being considered for various nuclear energy applications, and a road map for a code case involving several industrial partners has been proposed [26]. The alloy Haynes 282 (abbreviated 282 in this report) was also studied extensively in 2024 because of its very high strength at temperature up to 800°C [10, 11, 26, 27]. Although large printing defects were observed in the LPBF 282 creep specimens, the material was used to demonstrate that

advanced characterization techniques such as x-ray computed tomography (XCT) and micrograph image analysis can be used to assess the effect of LPBF process-induced flaws and limiting defects on the creep performance [28, 29]. The aim of this report is to summarize current knowledge on LPBF 282 and LPBF 625, discuss how the methodology developed for LPBF 282 to correlate process–microstructure–creep properties can be used for low-defect LPBF 625, and determine a path forward to deploy LPBF 625 in various nuclear reactors.

2. DEFECT ANALYSIS AND CREEP PERFORMANCE OF 282

2.1 FABRICATION AND MICROSTRUCTURE OF ANNEALED LPBF 282

Figure 1a shows the LPBF 282 build fabricated at the ORNL Manufacturing Demonstration Facility using a Renishaw AM250 machine. Process parameter optimization has been described elsewhere [9], and the following optimized printing parameters were used for building mechanical test specimens: laser power of 200 W, layer thickness of 60 µm, hatch spacing of 86 µm, point spacing of 70 µm, and exposure time of 80 ms. The powder chemistry provided by the manufacturer was as follows in weight percent: Ni–19.37Cr–10.24Co–8.33Mo–2.11Ti–1.54Al–0.05C–0.03Si–0.01O. The Renishaw AM250 was equipped with three imaging modalities—a 20 megapixel visible light camera, a 4.2 megapixel near-infrared camera, and a long-wave infrared camera—and examples of the generated in situ images are shown in Figure 2b. Spatter particles were observed during printing, more frequently for the C-specimen rods, and the formation of these spatter particles is illustrated in Figure 2c. The orientation of the build with respect to the Ar flow is the likely explanation for the higher density of spatter particles in the C-specimen region. The resulting microstructure is shown in Figure 2, with the presence of a high density of printing defects in the C1 specimen, as observed for all C specimens. The electron backscatter diffraction (EBSD) map presented in Figure 2c highlights the presence of a bimodal grain size distributed in the specimens annealed for 1 h at 1,180°C plus 4 h at 800°C (later referred to as HT), with very limited texture but elongated along the build direction (BD). Additional information can be found elsewhere [10, 11, 28, 29].

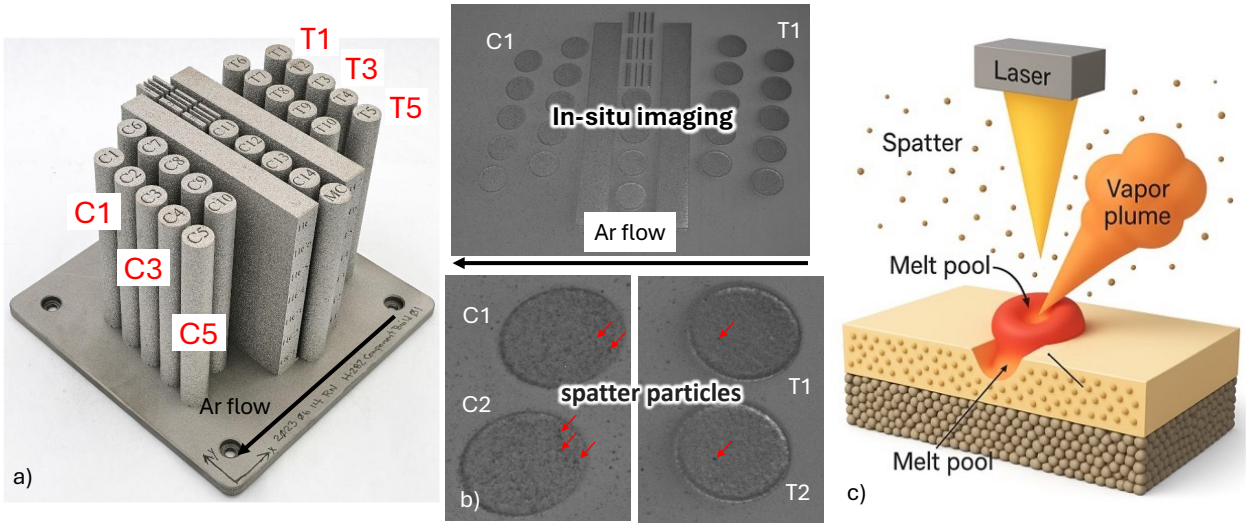

Figure 1. (a) LPBF 282 build fabricated using a Renishaw 250 machine, (b) in situ imaging during printing, and (c) AI-generated rendering of spatter particle formation during printing.

Scanning transmission electron microscopy characterization was conducted on the heat-treated T5 and C5 rods before creep testing. A high density of spherical, strengthening γ′ precipitates, ~50 nm in diameter, was observed for both the T5 and C5 specimens. Characterization was performed in the large-grain and small-grain areas for the T5 specimens, and no difference in γ′ size or dispersion was observed. The size

and distribution of γ′ precipitates are consistent with values reported for wrought 282 after the two-step or one-step heat treatments and should result in high creep strength [26, 27, 30, 31] up to ~800°C.

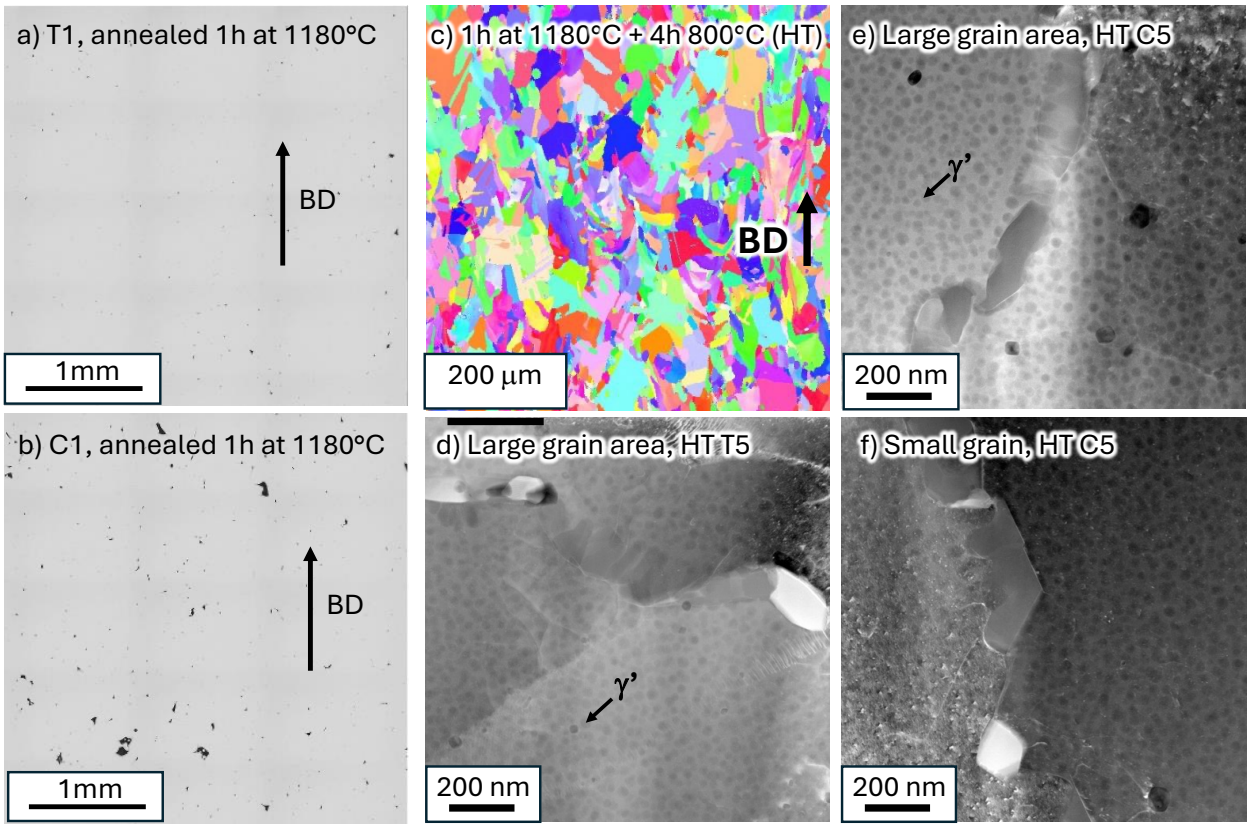

Figure 2. LPBF 282 microstructure and optical micrographs of rods (a) T1 and (b) C1 annealed for 1 h at 1,180°C. (c) EBSD map showing a bimodal grain size distribution. (d–f) Scanning transmission electron microscopy micrographs: (d) large-grain area, HT T5 rod; (e) large-grain area, HT C5 rod; and (f) small-grain area, HT C5.

2.2 CORRELATION BETWEEN CREEP PERFORMANCE AND DEFECTS

Figure 3a displays creep curves generated at 750°C, with applied stresses of 300 and 350 MPa for the T and C specimens. The measured lifetimes were about half what would be expected for wrought 282 and had significantly lower ductility, which was expected to be >20% for wrought 282 [27]. The C specimens exhibited lower ductility and slightly lower creep lifetimes compared with the T specimens. Nondestructive XCT was performed using a ZEISS Metrotom system with an x-ray source of 200 kV, and advanced deep learning–based algorithms were used in the 3D reconstruction, resulting in the detection limit of ~50 µm [11, 28, 29, 32]. The XCT reconstruction shown in Figure 3b of the C3 and T3 creep specimens before and after testing confirmed the higher density of printing defects in the C3 specimen compared with the T3 specimen [29]. A clear increase in measurable defects by XCT was observed for both specimens after creep testing. An additional XCT analysis of the T5 creep specimen is presented in Figure 4. Careful examination of the specimen before creep testing as well as after creep testing but before failure identified one large defect in the area where fracture will take place. A significant increase in the defect size was observed in the interrupted specimen after 546 h of testing and a deformation of 2.6%. The extent of the defect density translated to the reason for the rapid failure of the specimen once the test was restarted, with a strain to rupture of only 3%. Figure 4c shows the evolution of defects in the entire T5 specimen, revealing again a significant increase in defect density during creep. The red circles highlight an area where new defects were formed, some initial defects increased in size,

and some defects were barely affected by creep testing. Quantification of the defect size and shape evolution is ongoing.

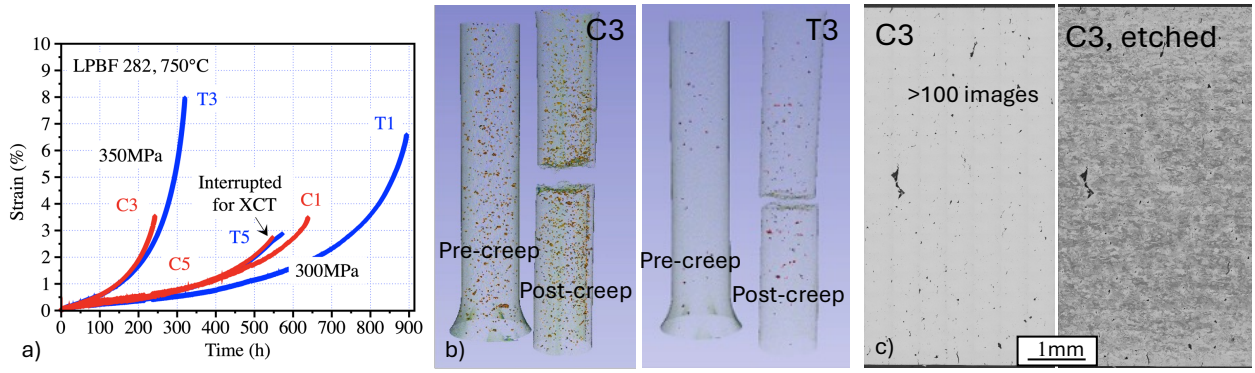

Figure 3. (a) Creep curves for the LPBF 282 at 750°C and applied stress of 300 or 350 MPa, (b) 3D XCT rendering of the C3 and T3 specimen before and after creep testing, and (c) optical mosaic micrographs of the as-polished and etched C3 specimens after creep testing.

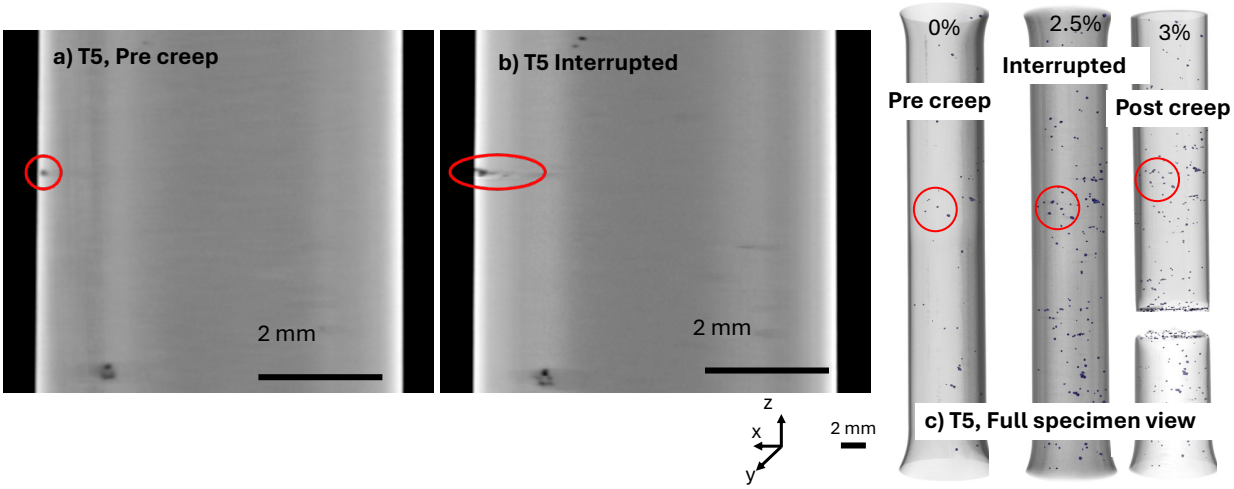

Figure 4. XCT data for the T5 specimen. (a) Precreep, critical defect; (b) interrupted creep test, critical defect evolution; and (c) full reconstruction of the T5 specimen, precreep, interrupted, and postcreep testing.

Analysis of over 100 optical images for each specimen in the gage and head using image analysis led to the conclusion that only two types of creep damage were observed: cavitation leading to cracking at grain boundaries (GBs) and cracks initiating from lack of fusion defects. Examples of these creep damages are shown in Figure 5a, with the extent of cracking from printed defects varying significantly from one defect to the other.

As shown in Figure 5b–Figure 5c, a simple classification based on defect circularity, with three categories—linear, circular, and irregular defects—demonstrated a significant increase in the linear defects due to cracking at GBs and irregular defects corresponding to cracks developing from LPBF process-induced defects. The complex shape of these cracks resulted in the Python code counting some of them as new irregular defects. This miscounting is the reason why an increase in both defect size and frequency is captured in Figure 5d, which were observed in the XCT reconstruction.

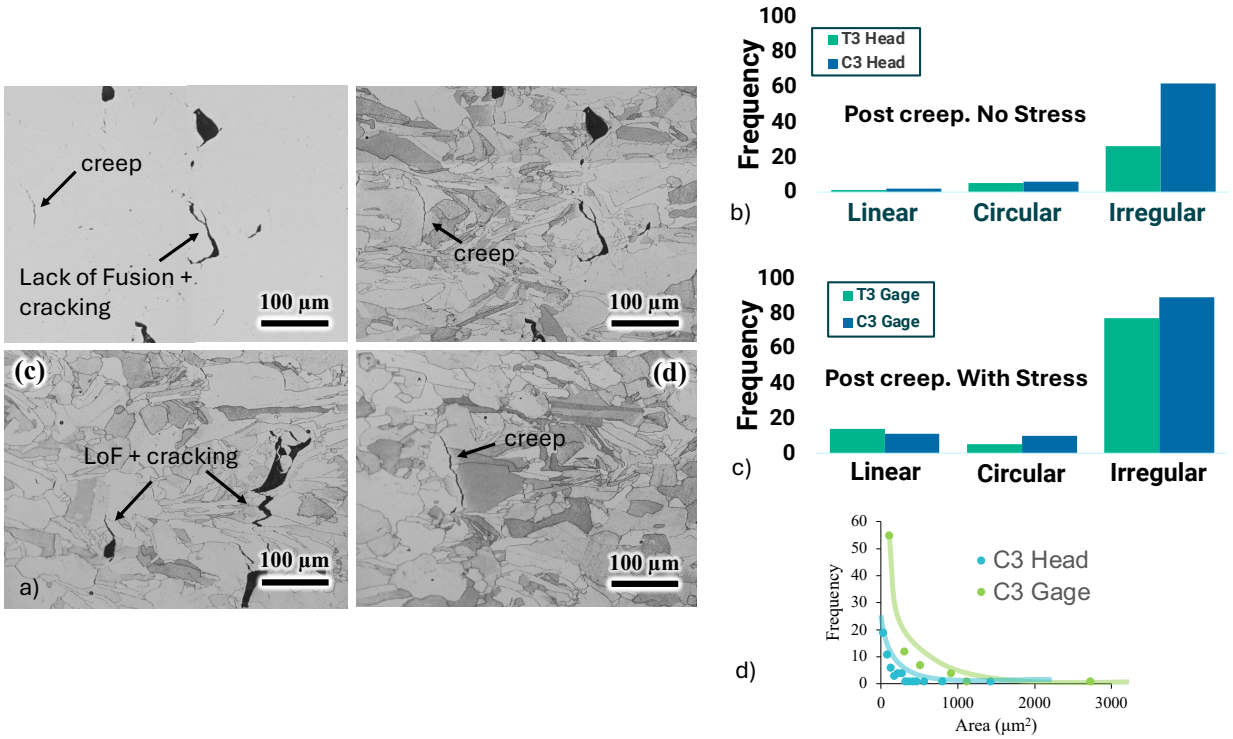

Figure 5. (a) Optical micrographs highlighting two types of creep damages in LPBF 282. Comparison of the defect density and type in the T3 and C3 specimens: (b) head and (c) gage. (d) Comparison of the defect population in the head and gage of the C3 specimen.

3. FABRICATION AND PERFORMANCE OF LPBF 625

3.1 PRINTABILITY AND DEFECT ANALYSIS

Several authors have demonstrated that 625 can be fabricated by LPBF with defect density lower than 99.9% [14]. This was confirmed by the authors' studies comparing the microstructure and room-temperature tensile properties of three solution-strengthened alloys—625, 230, and 617—fabricated using an LPBF Renishaw 250 machine [10, 11]. Although hot cracking was observed over a large window of printing parameters for the latter two alloys, crack-free LPBF 625 was produced with a low defect density. Extensive characterization of the three alloys can be found elsewhere [33], and LPBF 625 was selected for further investigation.

3.2 FABRICATION AND PEREGRINE ANALYSIS OF THE LPBF 625 BUILD

As shown in Figure 6, a large LPBF 625 build was printed on an EOS M290 with recycled Praxair Inconel 625 laser-cut powder and was designed with 15 cylindrical blanks with an outer diameter of 16 mm and height of 130 mm, alongside two blocks with dimensions of 130 × 13 × 130 mm. The EOS standard 625 parameters shown in Table 1 were used and melted with a flow optimized striping pattern rotating at 47° per layer and restriction angles of 30°. The powder chemistry was as follows: Ni–21.56Cr–8.81Mo–4Fe–3.73Nb–0.07Mn–0.06Co–0.02C–0.015O.

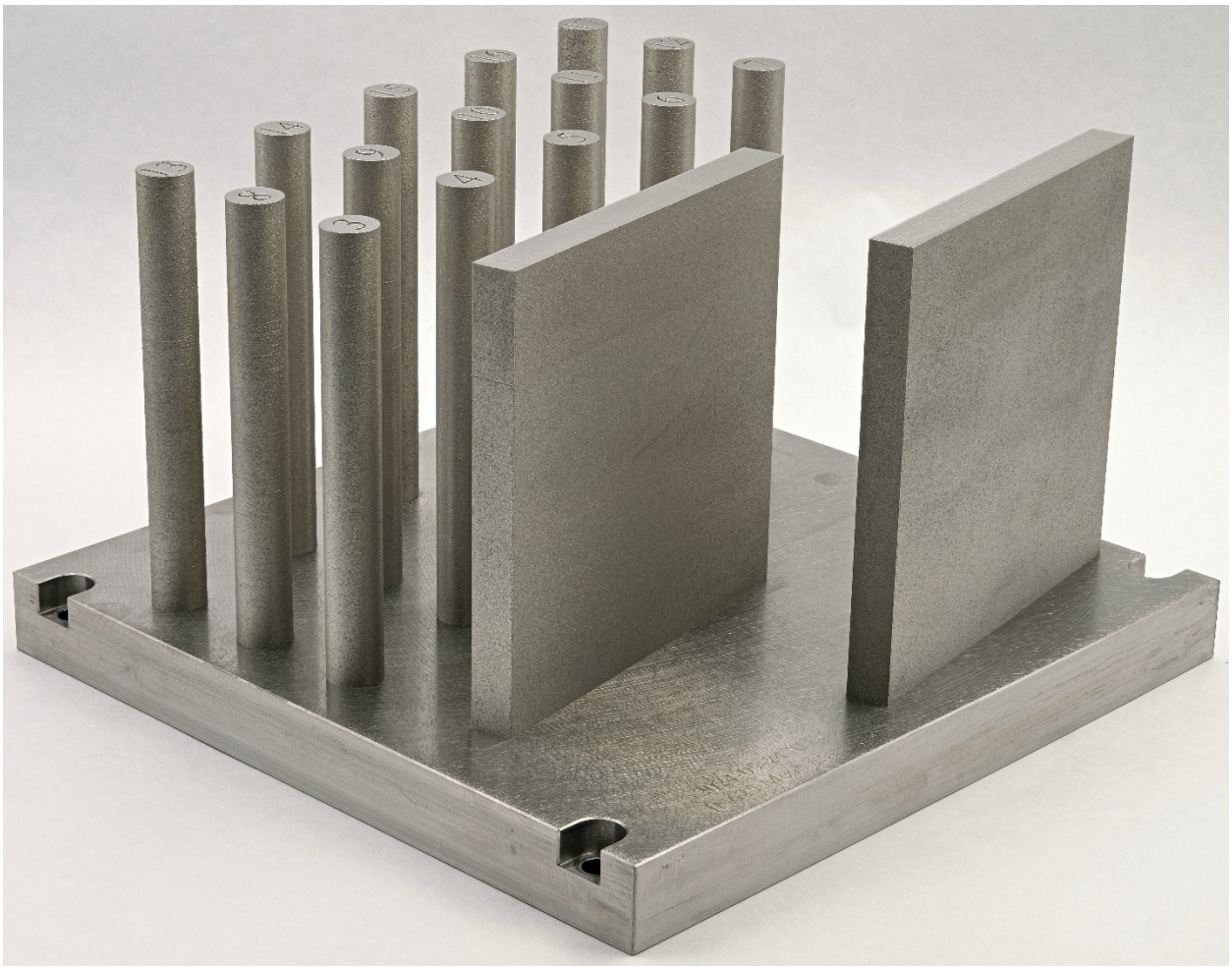

Figure 6. LPBF 625 build fabricated using an EOS M290 machine used for microstructure characterization and mechanical testing.

Table 1. Laser processing parameters for 625

Parameter	Value
Power	285 W
Velocity	960 mm/s
Hatch spacing	0.11 mm
Layer thickness	0.040 mm
Stripe width	10 mm

The EOS M290 was equipped with a 1 megapixel, grayscale, visible-light camera and a 5 megapixel thermal emissions near-infrared camera, both of which capture two images per layer. The visible-light camera captures one image after the layer has fused and one image after the subsequent layer has been recoated with powder. The thermal camera captures one time-integrated image and one maximum intensity value image during printing.

Peregrine is ORNL-developed software designed for powder bed fusion AM processes and allows users to collect, analyze, and visualize in situ sensor and ex situ characterization data to assist engineers when

making build or part quality determinations during or after printing [34]. For the EOS M290 system, data are collected and analyzed using a user-trained dynamic multilabel segmentation convolutional neural network (DMSCNN), which points operators to regions of interest within the build. Each pixel is given a label from a list of user-defined labels to classify each pixel—for example, *Powder* or *Printed*.

Figure 7 shows a heat map of Printed class detections through build height normalized by each part's volume within the build. Note that P1 does not appear because it is the plate label. All the parts appear at 100% detection, indicating they were perfectly printed. A second heat map for every class detection except *Powder* and *Printed* is presented in Figure 8. P18 exhibited a large number of flaws, but further analysis revealed many of these detections were false positives. This issue will be improved by further training of the DMSCNN.

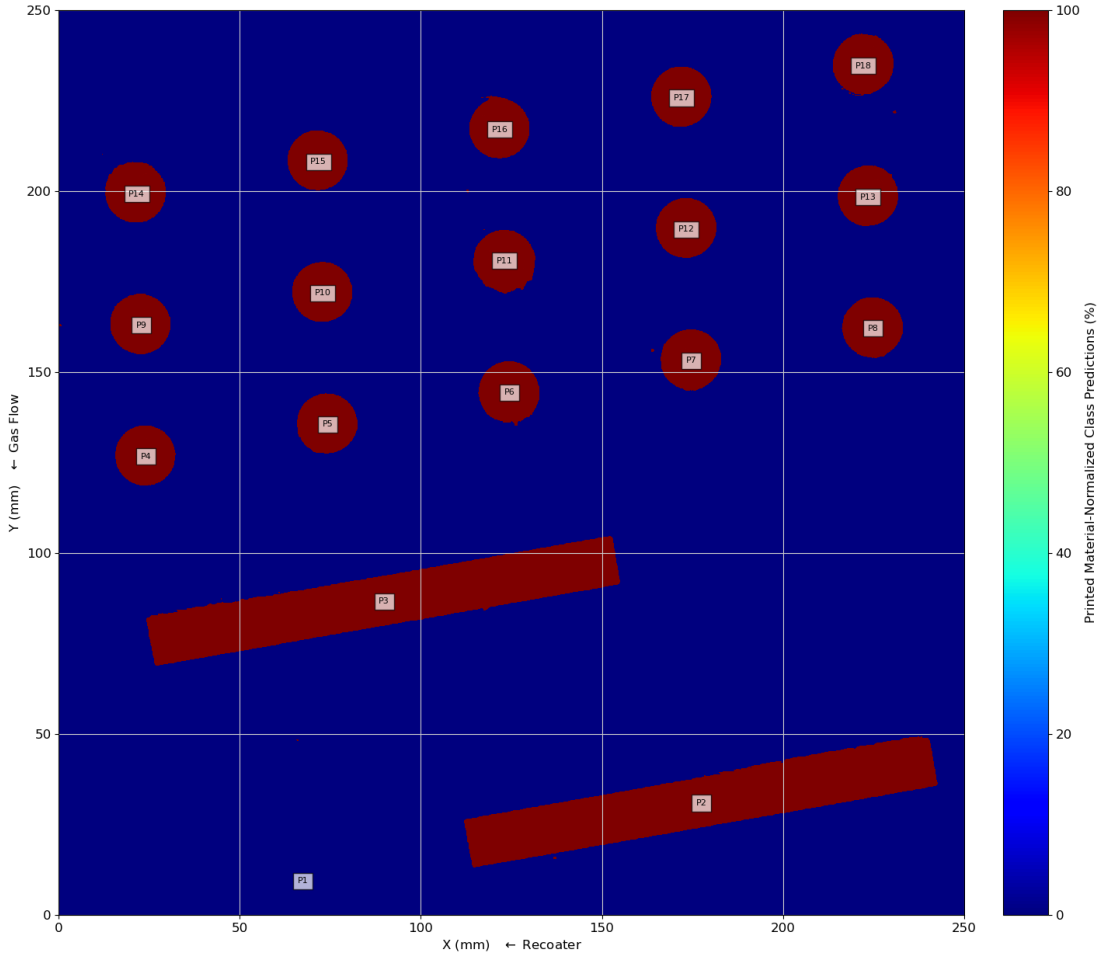

Figure 7. Heat map of Printed class detections normalized by each part's volume within the build. Note that P1 does not appear because it is the plate label.

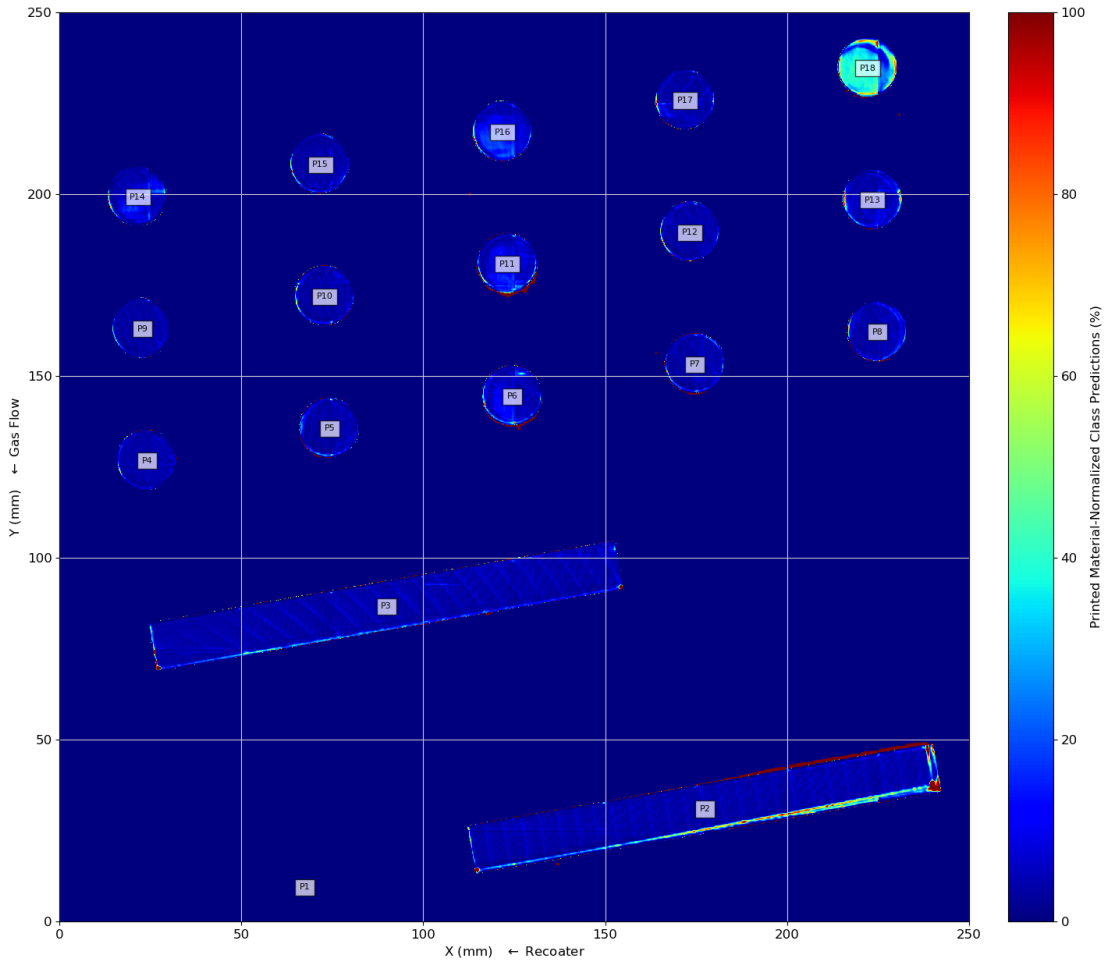

Figure 8. Heat map for every class detection except *Powder* and *Printed* normalized by each part's volume within the build.

4. CHARACTERIZATION OF AS-PRINTED AND ANNEALED LPBF 625

4.1 MICROSTRUCTURE OF LPBF 625

Many studies have assessed the effect of heat treatment on the microstructure and properties of LPBF 625. Two categories of heat treatments were considered in this study: stress relief between 600°C and 900°C [16–20] and solution annealing above 1,000°C [15–17, 22]. Although 870°C is a typical stress relief treatment recommended by industry for LPBF 625 [19, 35], several authors have observed the rapid formation of the brittle δ phase; temperature–time–transformation (TTT) diagrams for the δ phase formation in LPBF 625 have been generated, finding considerable deviation from similar TTT curves for wrought material [21]. Due to the segregation in the interdendritic zone inherent to the rapid solidification during LPBF, studies found that the formation of the δ phase was two orders of magnitude faster for LPBF 625 compared with wrought 625. Successful homogenization of the LPBF 625 microstructure and grain recrystallization were achieved after exposure for 1 or 2 h at 1,150°C [15–17]. Because the optimized stress relief heat treatment for LPBF 625 has not been clearly established yet, the focus in this study was on the as-printed and solution-annealed LPBF 625.

EBSD maps of the LPBF 625 alloy in the conditions of as-printed and annealed at 1,150°C for 1 or 4 h are compared in Figure 9. The as-printed material exhibited elongated, textured grains along the BD with an average diameter of 15.8 µm [14, 16, 18, 24]. The kernel average misorientation and grain orientation spread maps revealed a significant decrease in overall dislocation density and strain within the grains after solution annealing at 1,150°C. Texture became more randomized, and the presence of Σ3 annealing twins and the microstructural changes indicate full recrystallization occurred after 1 h at 1,150°C [15–17, 22]. Moreover, a statistically significant difference was not present in grain areas (not including the twins) between 1 and 4 h of annealing. As shown in Figure 10, after solution annealing for 1 h at 1,150°C, the cellular structure disappeared, and small precipitates (~0.003 µm^2) formed along the GBs. After 4 h of solution annealing, the precipitates coarsened and increased to an area of approximately 0.5 µm^2. In the as-printed condition, the energy-dispersive X-ray spectroscopy (EDS) elemental maps reveal segregation of Mo and Nb at the cellular structure level [15, 17–19]. However, after 1 h of solution annealing, the Mo and Nb segregation in the cell walls disappeared, and precipitates enriched in Mo and Nb were only observed at GBs (Figure 11).

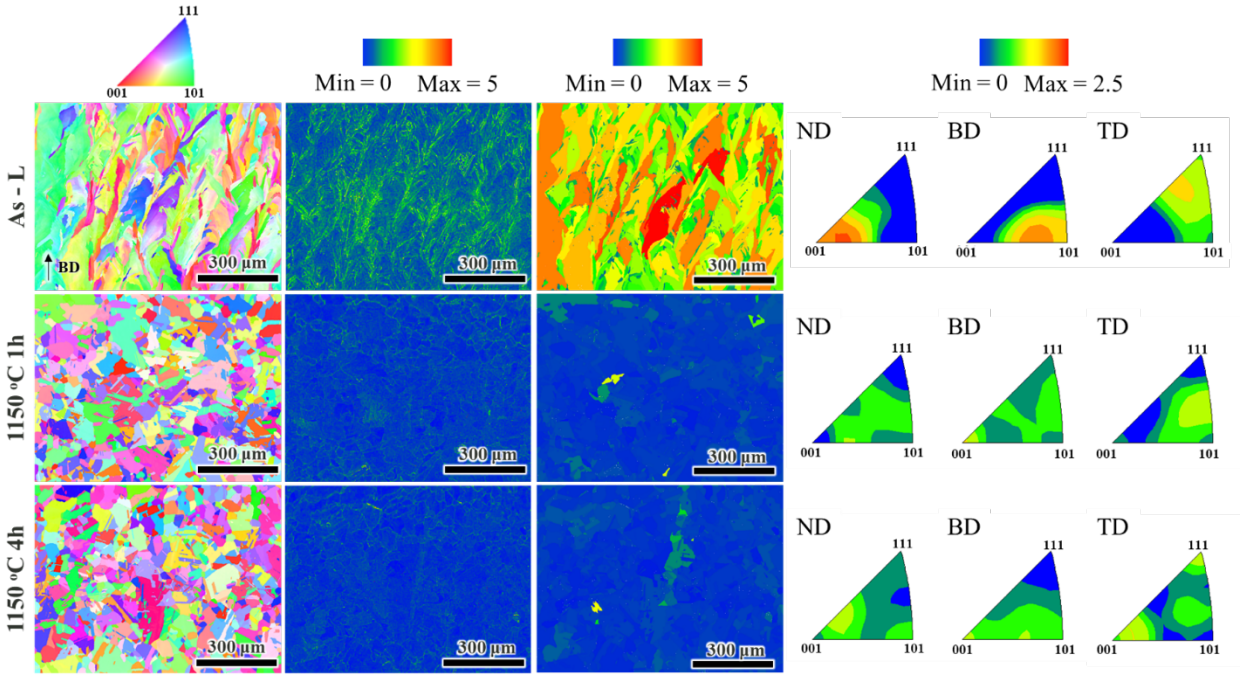

Figure 9. EBSD orientation, kernel average misorientation, grain orientation spread, and texture maps for LPBF 625 in the as-printed condition and solution annealed at 1,150°C for 1 and 4 h.

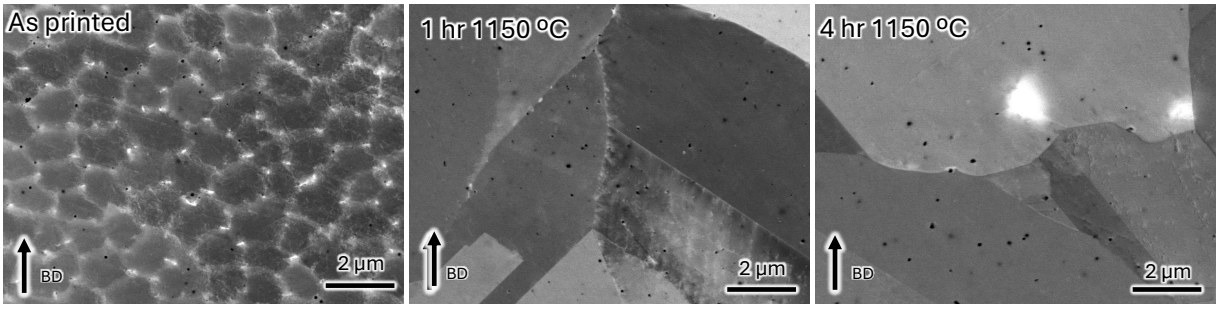

Figure 10. Backscattered electron–scanning electron microscopy micrographs of LPBF 625 in the as-printed condition and solution annealed at 1150°C for 1 and 4 h.

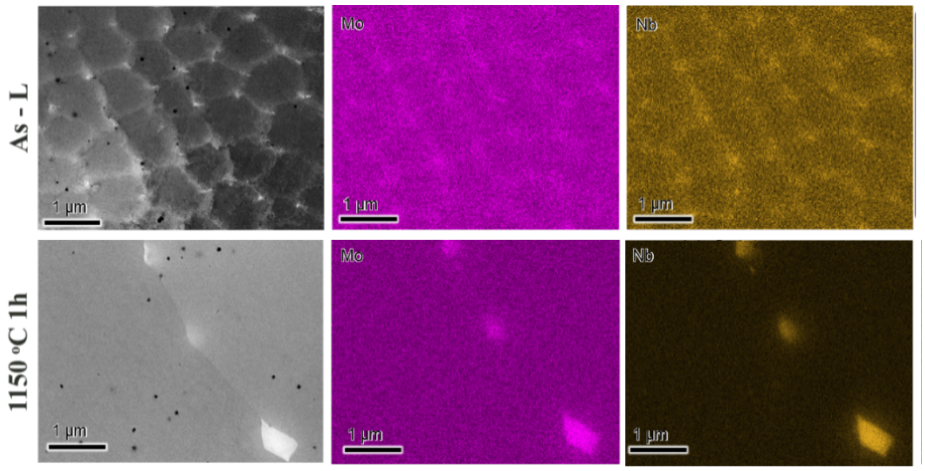

Figure 11. Backscattered electron–scanning electron microscopy micrographs and the corresponding EDS elemental maps for LPBF 625 in the as-printed condition and solution annealed at 1,150°C for 1 h.

4.2 ROOM-TEMPERATURE TENSILE PROPERTIES

Tensile testing was conducted at room temperature on small-scale dog bone specimens with a gage section of 2 × 2 mm and a gage length 7.62 mm. The size of the specimens prevented the use of an extensometer, and the yield strength (YS), ultimate tensile strength (UTS), and plastic deformation were calculated from the crosshead displacement. Tensile curves for the as-printed and 1 h, 1,150°C annealed specimens are shown Figure 12 for specimens machined along and perpendicular to the BD. These curves were used to calculate the YS, UTS, and plastic strain at rupture, presented in Table 2. Anisotropic tensile properties were observed for the as-printed LPBF 625 with lower strain at rupture but higher YS and UTS for the specimen tested perpendicular to the BD. Annealing for 1 h at 1,150°C resulted in a significant decrease in YS, consistent with the disappearance of dislocations reported in Figure 9. Interestingly, recrystallization after 1 h at 1,150°C resulted in isotropic tensile properties at room temperature, as illustrated by the very similar tensile curves along and perpendicular to the BD after 1 h at 1,150°C. Tensile testing was also conducted on two specimens machined along the BD and annealed for 4 h at 1,150°C. A very slight decrease in YS and UTS was observed compared with the results for the 1 h, 1,150°C specimens, consistent with the limited grain grown measured after 4 h at 1,150°C compared with 1 h exposure. Many studies have looked at the effect of heat treatments on the LPBF 625 tensile properties [14, 20, 22, 24], and data from Marchese et al. [16] are summarized in Table 3. The present study's results are consistent with the published results in the conditions of as-printed and annealed for 2 h at 1,150°C, but this study found more elongation at rupture. The solution anneal appeared to have homogenized the LPBF 625, as demonstrated by similar tensile behavior both parallel and perpendicular to the BD; this was also reported by Kreitcberg et al. [24] after solution annealing or hot isostatic pressing, but temperature and pressure were not communicated to protect proprietary information. Trends between Kreitcberg et al. [24] and the current work were similar at room temperature, but again, strains at rupture were lower than that measured in the present study. Surprisingly, Kreitcberg et al. [24] reported a drastic decrease in ductility at temperatures >650°C for both the as-printed and solution-annealed materials, which was not observed for wrought 625. Testing of the present study's LPBF 625 material will therefore be conducted at high temperature in the coming weeks.

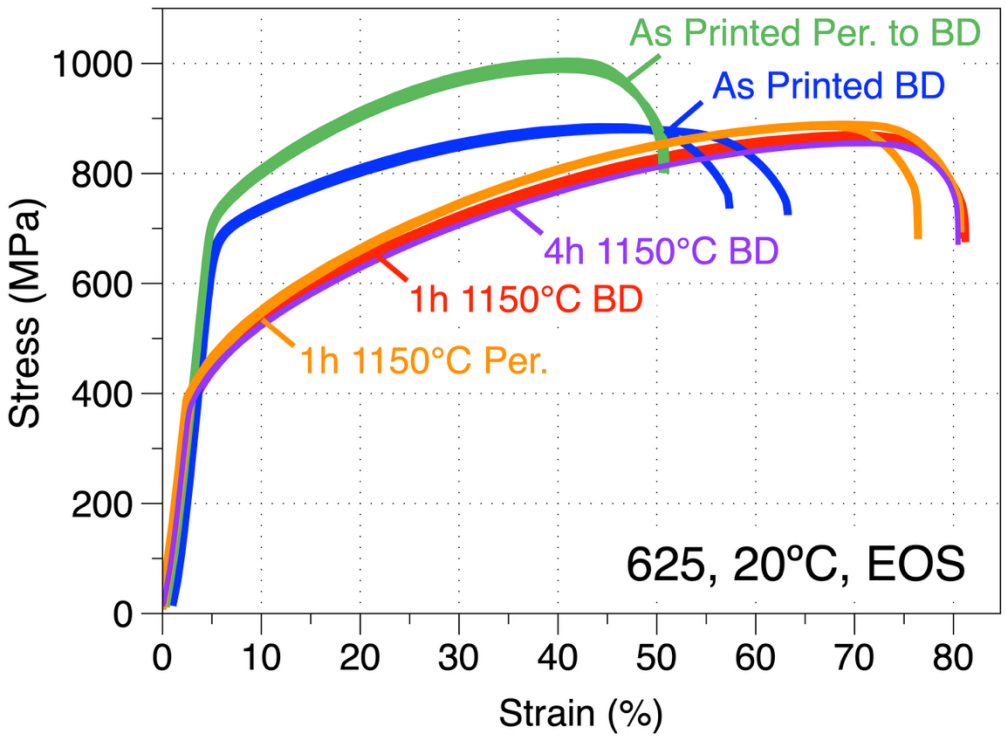

Figure 12. Tensile curves at room temperature for LPBF 625 specimens in the as-printed and 1,150°C annealed conditions machined along and perpendicular to the BD.

Table 2. Room-temperature mechanical properties of the LPBF 625 specimens along and perpendicular to (Perp.) the BD in the as-printed and 1,150°C annealed conditions

Condition	Orientation	YS (MPa)	UTS (MPa)	Plastic strain (%)
As-printed	BD	640.3	884.6	53.3
As-printed	BD	641.7	880.2	59.2
As-printed	Perp. BD	695.6	989.7	45.9
As-printed	Perp. BD	705.5	1003.8	45.7
1 h, 1,150°C	BD	389.56	870.08	78
1 h, 1,150°C	BD	387.4	864.17	78.29
1 h, 1,150°C	Perp. BD	399.72	886.37	73.28
1 h, 1,150°C	Perp. BD	399.23	888.99	78.06
4 h, 1,150°C	BD	379.7	854.5	77.5
4 h, 1,150°C	BD	381.2	856.29	77.27

Table 3. Room-temperature mechanical properties of the LPBF 625 specimens along and perpendicular to (Perp). the BD in the as-printed; 1 h, 870°C annealed; and 2 h, 1,150°C annealed conditions from Marchese et al. [16]

Conditions	Orientation	YS (MPa)	UTS (MPa)	Plastic strain (%)
As-printed	BD	618 ± 33	891 ± 5	40.7 ± 0.5
As-printed	Perp. BD	783 ± 23	1,041 ± 36	33.1 ± 0.6
1 h, 870°C	BD	621 ± 7	900 ± 2	40.9 ± 1.7
1 h, 870°C	Perp. BD	667 ± 3	996 ± 3	35.8 ± 1.8
2 h, 1,150°C	BD	379 ± 9	851 ± 3	54.5 ± 1.1
2 h, 1,150°C	Perp. BD	396 ± 9	883 ± 15	54.9 ± 1.2

5. CREEP TESTING AT 725°C

Creep testing was conducted at 725°C because a broad range of data were generated at that temperature on LPBF stainless steel 316H, and this temperature is close to the maximum temperature considered for the wrought 625 code case (i.e., 750°C). Two tests were initiated on as-printed standard cylindrical specimens machined along the BD with a gage length of 32 mm and a gage section 0.63 mm in diameter. The goal of these experiments was to assess the possibility to follow damage evolution via XCT measurements every 1,000 h. The 150 and 125 MPa were selected to reach estimated lifetimes of 2,500 and 5,000 h, respectively, based on wrought 625 data. The ongoing creep curves shown in Figure 13a exhibit very low creep rates after 1,600 h, suggesting that the lifetimes are likely to exceed the original 2,500 and 5,000 h estimates. XCT renderings of the specimen tested at 150 MPa in the as-printed condition and after creep testing for 1,000 h are displayed in Figure 13b. In both cases, no defect could be detected, in contrast with previous characterization of the LPBF 282 specimens. The next creep test interruption will take place after 3,000 h, and measurements will be conducted on a Zeiss Versa XCT system with an expected resolution of approximately 7 μm to be compared with the 17 μm resolution for the Metrotom system.

Three creep tests were initiated at 725°C and 200 MPa using small-scale dog bone specimens with a geometry similar to the geometry used for tensile testing. Testing was conducted on specimens machined parallel to the BD in the as-printed and 1 h, 1,150°C annealed conditions, and the ongoing creep curves are displayed in Figure 14a. In both cases, a long, complex primary creep stage was observed, resulting in continuously decreasing creep rates after approximately 100 h of exposure. One as-printed specimen polished to a 1 μm finish was tested in vacuum for 100 h in the same condition (i.e., 725°C, 200MPa), and scanning electron microscopy surface characterization is presented in Figure 14b and Figure 14c. The cellular structure was still present with an increase in the carbide volume fraction at the GBs and in the cell walls. Fine, needle-like precipitates rich in Nb were also observed, consistent with the formation of δ-phase precipitates reported by many authors for LPBF 625 after heat treatment at 700°C–900°C. These precipitates were also observed by Son et al. [36] for the solution-annealed LPBF 625 after short-term creep testing at 800°C and by Pasiowiec et al. [37] after creep testing at 600°C and 700°C for 2,000 h, 750°C for 520 h, and 800°C for 240 h and for LPBF 625 stress relief for 1 h at 980°C. They concluded that the high density of δ phase strengthened the LPBF 625 at 700°C–750°C compared with wrought 625, but at 800°C, coarsening of the δ phase, carbides, and Laves phase at GBs led to GB cavitation and resulting low ductility.

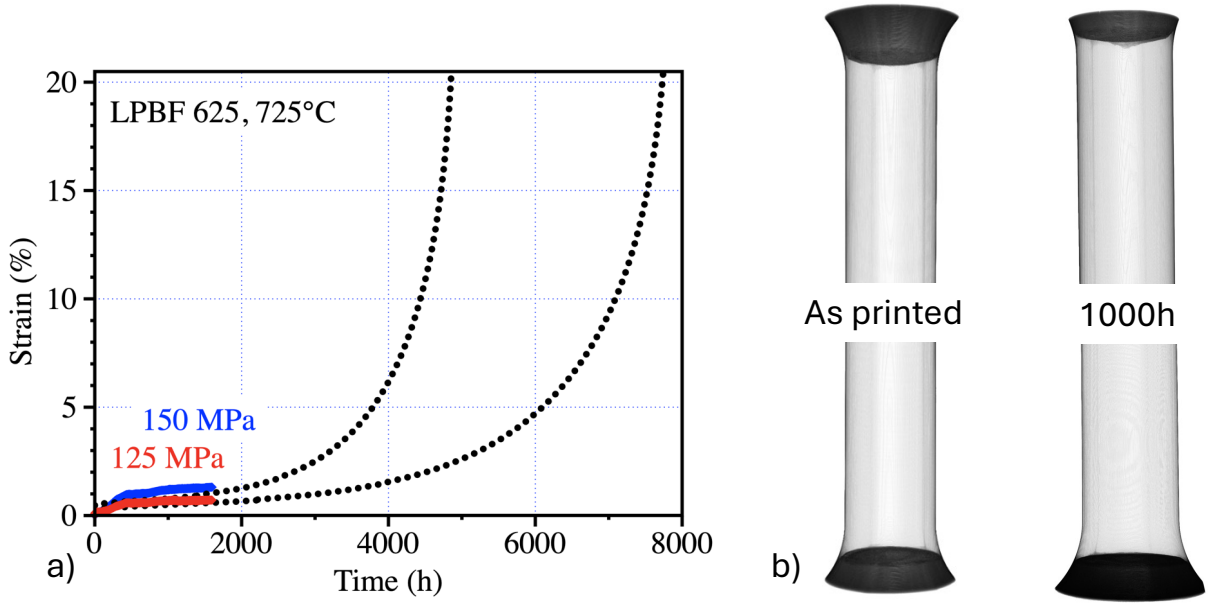

Figure 13. (a) Ongoing creep curves for as-printed LPBF 625 specimens tested at 725°C and 125 or 150 MPa and (b) XCT 3D rendering of the specimens tested at 150 MPa in the as-printed condition and after creep testing for 1,000 h.

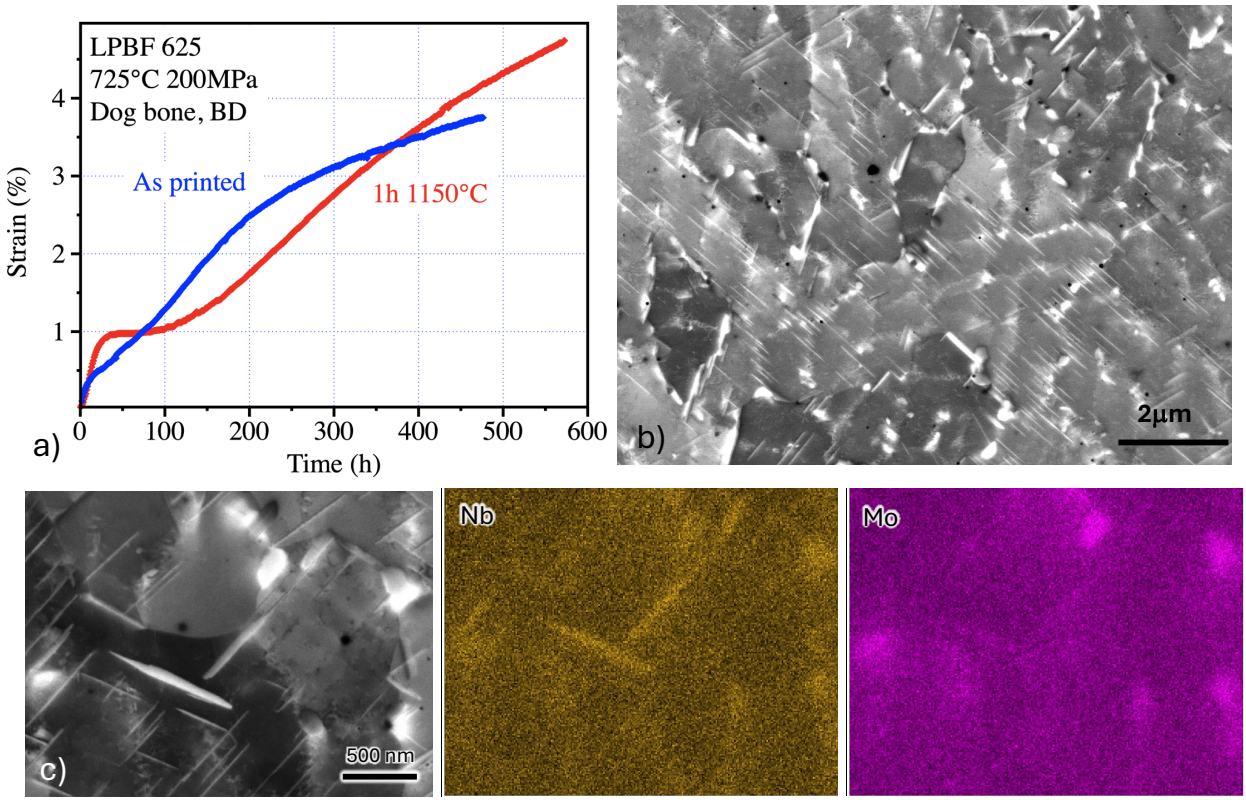

Figure 14. (a) Ongoing creep curves at 725°C and 200 MPa for the as-printed and 1 h, 1,150°C annealed LPBF 625, (b) micrographs of a specimen creep tested in vacuum at 725°C and 200 MPa for 100 h; and (c) EDS maps highlighting Nb- and Mo-rich precipitates in (b).

6. CONCLUSION

Because of their relevance to the nuclear energy industry, this study examined alloys 282 and 625 fabricated by LPBF. Although a high density of strengthening δ′ precipitates was achieved after heat treating the LPBF 282 at 1,180°C for 1 h and 800°C for 4 h, the alloy exhibited lower lifetime and ductility compared with wrought 282 because of the presence of large printing defects. Using XCT and microstructural characterization combined with data analytics, two types of creep damage could be quantified at 750°C, as well as cracks initiated at printed defects and cavitation followed by cracking at GBs. Contrary to the results for LPBF 282, a very low defect density was achieved for LPBF 625, and no defects were detected in creep specimens using an XCT system with a resolution of ~50 μm. Creep testing conducted at 725°C on as-printed 625 revealed creep strength superior to the creep strength of wrought 625, but a longer testing duration is needed to evaluate the alloy creep ductility. Rapid formation of small, needle-like δ-phase precipitates were observed after creep testing for 100 h at 725°C, consistent with the literature and likely due to the initial Nb and Mo segregation in the LPBF 625 cell walls. Solution annealing for 1 h at 1,150°C resulted in full recrystallization of the alloy and led to isotropic tensile properties at room temperature, with a significant decrease in YS but an increase in ductility compared with the as-printed LPBF 625.

7. REFERENCES

1. I. Gibson, D. Rosen, B. Stucker, M. Khorasani, *Additive Manufacturing Technologies*, Vol. 17 (Springer, 2021).
2. J. Haley, C. Leach, B. Jordan, R. Dehoff, and V. Paquit, "In-Situ Digital Image Correlation and Thermal Monitoring in Directed Energy Deposition Additive Manufacturing," *Optics Express* 29, no. 7 (2021): 9927–9941.
3. A. Huning, A. Smith, L. Scime, M. Russell, A. Coates, V. Paquit, and R. Dehoff, *Advancement of Certification Methods and Applications for Industrial Deployments of Components Derived from Advanced Manufacturing Technologies*, ORNL/TM-2022/2654 (Oak Ridge National Laboratory, 2022).
4. M. Li, , R. Dehoff, A. Jokisaari, M. D. McMurtrey, I. J. Van Rooyen, and D. Cairns-Gallimore, *Advanced Materials and Manufacturing Technologies (AMMT) 2025 Roadmap*, ANL-24/70 (Argonne National Laboratory, 2025).
5. A. Ziabari, et al., *Report Outlining Computed Tomography Strategy and Microscopy Approach to Qualifying AM 316 Materials*, ORNL/TM-2023/3016 (Oak Ridge National Laboratory, 2023).
6. X. Zhang, S. A. Mantri, G. I. Vukovic, J. Listwan, D. Rink, and E. Listwan, *Development of Process Parameters and Post-Build Conditions for Qualification of LPBF 316 SS*, ANL-AMMT-004 (Argonne National Laboratory, 2023).
7. P. Nandwana, S. Dryepondt, C. Massey, S. Bell, S. Nayir, G. Kumari, and C. Joslin, *Deposit and Evaluate Material Across Extremes of Process Windows*, ORNL/TM-2025/3789 (Oak Ridge National Laboratory, 2025).
8. M. Griffiths, "Chapter 9: Ni-Based Alloys for Reactor Internals and Steam Generator Applications," in *Structural Alloys for Nuclear Energy Applications*, ed. G. R. Odette and S. J. Zinkle (Elsevier, 2019).
9. S. Dryepondt, et al., *Prioritization of Existing Reactor Materials*, ORNL/TM-2023/3108 (Oak Ridge National Laboratory, 2023).

10. S. Dryepondt, et al., *Complete Optimization of Laser Powder Bed Fusion Nickel-Based Alloys Downselected from FY 2023 Candidate Materials Including Thermodynamic Modeling, Sample Fabrication, and Microstructure Characterization*, ORNL/TM-2024/3464 (Oak Ridge National Laboratory, 2024).
11. S. Dryepondt et al., *Evaluation of DED and LPBF Ni-Based Alloys Process Application Envelopes Based on Performance, Process Economics, Supply Chain Risks and Reactor-Specific Targeted Components*, ORNL/TM-2024/3604 (Oak Ridge National Laboratory, 2024).
12. I. Yadroitsev, L. Thivillon, Ph. Bertrand, and I. Smurov, "Strategy of Manufacturing Components with Designed Internal Structure by Selective Laser Melting of Metallic Powder," *Applied Surface Science* 254 (2007): 980–983.
13. I. Yadroitsev, M. Pavlov, P. Bertrand, and I. Smurov, "Mechanical Properties of Samples Fabricated by Selective Laser Melting," 14èmes Assises Européennes du Prototypage and Fabrication Rapide, June 24–25, 2009.
14. H. Wong, K. Dawson, G. A. Ravi, L. Howlett, R. O. Jones, and C. J. Sutcliffe, "Multi-Laser Powder Bed Fusion Benchmarking-Initial Trials with Inconel 625," *International Journal of Advanced Manufacturing Technology* 105 (2019): 2891–2906.
15. G. Marchese, M. Lorusso, S. Parizia, E. Bassini, J. W. Lee, F. Calignano, D. Manfredi, M. Terner, H. U. Hong, D. Ugues, M. Lombardi, and S. Biamino, "Influence of Heat Treatments on Microstructure Evolution and Mechanical Properties of Inconel 625 Processed by Laser Powder Bed Fusion," *Materials Science and Engineering A: Structural Materials, Properties, Microstructure and Processing* 729 (2018): 64–75.
16. G. Marchese et al., "The Role of Texturing and Microstructure Evolution on the Tensile Behavior of Heat-Treated Inconel 625 Produced via Laser Powder Bed Fusion," *Materials Science and Engineering A: Structural Materials, Properties, Microstructure and Processing* 769 (2020): 138500.
17. F. Zhang, L. E. Levine, A. J. Allen, C. E. Campbell, E. A. Lass, S. Cheruvathur, M. R. Stoudt, M. E.Williams, and Y. Idell, "Homogenization Kinetics of a Nickel-Based Superalloy Produced by Powder Bed Fusion Laser Sintering," *Scripta Materialia* 131 (2017): 98–102.
18. F. Zhang, L. E. Levine, A. J. Allen, M. R. Stoudt, G. Lindwall, E. A. Lass, M. E. Williams, Y. Idell, and C. E. Campbell, "Effect of Heat Treatment on the Microstructural Evolution of a Nickel Based Superalloy Additive-Manufactured by Laser Powder Bed Fusion," *Acta Materialia* 152 (2018): 200–214.
19. E. A. Lass, M. R. Stoudt, M. E. Williams, M. B. Katz, L. E. Levine, T. Q. Phan, T. H. Gnaeupel-Herold, and D. S. NG, "Formation of the Ni_3Nb δ-Phase in Stress-Relieved Inconel 625 Produced via Laser Powder-Bed Fusion," *Metallurgical and Materials Transactions A: Physical Metallurgy and Materials Science* 48 (2017): 5547–5558.
20. M. R. Stoudt, E. A. Lass, D. S. NG, M. E. Williams, F. Zhang, C. E. Campbell, G. Lindwall, and L. E. Levine, "The Influence of Annealing Temperature and Time on the Formation of d-Phase in Additively-Manufactured Inconel 625," *Metallurgical and Materials Transactions A: Physical Metallurgy and Materials Science* 49 (2018): 3028–3027.
21. G. Lindwall, C. E. Campbell, E. A. Lass, F. Zhang, M. R. Stoudt, A. J. Allen, and L. E. Levine, "Simulation of TTT Curves for Additively Manufactured Inconel 625," *Metallurgical and Materials Transactions A: Physical Metallurgy and Materials Science* 50 (2019): 457–467.
22. J. Nguejio, F. Szmytka, S. Hallais, A. Tanguy, S. Nardone, and M. Godino Martinez, "Comparison of Microstructure Features and Mechanical Properties for Additive Manufactured and Wrought

Nickel Alloys 625," *Materials Science and Engineering A: Structural Materials, Properties, Microstructure and Processing* 764, 138214 (2019).

23. J. Lee, M. Terner, S. Jun, H.-U. Hong, E. Copin, and P. Lours, "Heat Treatments Design for Superior High-Temperature Tensile Properties of Alloy 625 Produced by Selective Laser Melting," *Materials Science and Engineering A: Structural Materials, Properties, Microstructure and Processing* 790 (2020): 139720.
24. A. Kreitcberg, K. Inaekyan, S. Turenne, and V. Brailovski, "Temperature- and Time-Dependent Mechanical Behavior of Post-treated IN625 Alloy Processed by Laser Powder Bed Fusion," *Journal of Manufacturing and Materials Processing* 3 (2019): 75.
25. H. Mahajan, M. McMurtrey, M. Messner, and B. Barua, *Alloy 625 Qualification Pathway for ASME Section III Division 5 Class A construction*, INL/RPT-25-85288 (Idaho National Laboratory, 2025).
26. L. M. Pike, "Development of a Fabricable Gamma-Prime (γ′) Strengthened Superalloy," in *Superalloys*, ed. R. C. Reed, K. A. Green, P. Caron, T. P. Gabb, M. G. Fahrmann, E. S. Huron, and S. A. Woodard (The Minerals, Metals and Materials Society, 2008), 191–200.
27. B. A. Pint, H. Wang, C. S. Hawkins, and K. A. Unocic, *Technical Qualification of New Materials for High Efficiency Coal-Fired Boilers and Other Advanced FE Concepts: Haynes 282 ASME Boiler and Pressure Vessel Code Case*, ORNL/TM-2020/1548 (Oak Ridge National Laboratory, 2020).
28. S. Dryepondt, H. Hyer, F. List III, S. Taller, A. Ziabari, Yi-Feng Su, and Z. Snow, "Microstructure and Mechanical Properties of Ni-based Alloys Fabricated by Laser Powder Bed Fusion," *Proceedings from 10th International Conference on Advances in Materials, Manufacturing and Repair for Power Plants*, Indian Wells, California, February 25–28, 2025, EPRI and ASM International.
29. H. Hyer, A. Heimbrook, R. Franklin, A. Ziabari, and S. Dryepondt, "Relating Process Anomalies from Laser Powder Bed Fusion on Ni282 to Creep Deformation," *Advanced Materials and Processes* 183 (2025): 11–16.
30. Shen, C., *Modeling Creep-Fatigue-Environment Interactions in Steam Turbine Rotor Materials for Advanced Ultra-supercritical Coal Power Plants*, GE Global Research Final Report, DOE/NETL Cooperative Agreement DE-FE0005859 (US Department of Energy, 2014).
31. K. A. Unocic, D. Shin, X. Sang, E. Cakmak, and P. F. Tortorelli, "Single-Step Aging Treatment for a Precipitation-Strengthened Ni-Based Alloy and Its Influence on High-Temperature Mechanical Behavior," *Scripta Materialia* 162 (2019): 416–420.
32. A. Ziabari, et al. "Enabling Rapid X-Ray CT Characterization for Additive Manufacturing Using CAD Models and Deep Learning-Based Reconstruction," *npj Computational Materials* 9, no. 91 (2023).
33. A. Heimbrook, H. Hyer, and S. Dryepondt, "Effect of Chemistry and Laser Powder Bed Fusion Processing Parameters on the Solidification and Microstructure of Solid-Solution Strengthened Ni-Based Alloys," submitted to *Additive Manufacturing*.
34. S. Seay, "AI Software Enables Real-Time 3D Printing Quality Assessment," Oak Ridge National Laboratory, August 13, 2020, https://www.ornl.gov/news/ai-software-enables-real-time-3d-printing-quality-assessment.
35. EOS, *EOS NickelAlloy IN625 Material Data Sheet*, https://www.eos.info/05-datasheet-images/Assets_MDS_Metal/EOS_NickelAlloy_IN625/Material_DataSheet_EOS_NickelAlloy_IN625_en.pdf.

36. K. T. Son, T. Q. Phan, L. E. Levine, K. S. Kim, K. A. Lee, M. Ahlfors, and M. E. Kassner, “The Creep and Fracture Properties of Additively Manufactured Inconel 625,” *Materialia* 15 (2021).

37. H. Pasiowiec, B. Dubiel, R. Dziurka, P. Bała, P. Ledwig, M. Wrobel, M. Gajewska, W. Ziaja, and M. Poręba, “Effect of Creep Deformation on the Microstructure Evolution of Inconel 625 Nickel-Based Superalloy Additively Manufactured by Laser Powder Bed Fusion,” *Materials Science and Engineering A: Structural Materials, Properties, Microstructure and Processing* 887 (2023): 145742.